Research Article

Nano Research
2022, 15(7): 6168–6175

ISSN 1998-0124 CN 11-5974/O4
https://doi.org/10.1007/s12274-022-4264-z

Construction of three-dimensional carbon framework-loaded silicon nanoparticles anchored by carbon film for high-performance lithium-ion battery anode materials

Fan Wu[1], Zhichao He[1], Mingqiang Wang[1,3] (✉), Yudong Huang[1], and Fei Wang[1,2] (✉)

[1] *School of Chemistry and Chemical Engineering, Harbin Institute of Technology, Harbin 150001, China*
[2] *State Key Laboratory of Electroanalytical Chemistry, Changchun Institute of Applied Chemistry, Chinese Academy of Sciences, Changchun 130022, China*
[3] *Jiangsu Province Key Laboratory of Fine Petrochemical Engineering, Changzhou University, Changzhou 213164, China*

Received: 20 December 2021 / **Revised:** 19 February 2022 / **Accepted:** 21 February 2022

ABSTRACT

Si materials are widely considered to be the next-generation anode to replace the current commercial graphite-based anode due to its high energy density. However, the large volume variation of silicon during (de)lithiation process leads to rapid capacity decay, hindering its commercial application. Although the various hollow structure designs of Si nanomaterials have improved their cycling stability in the laboratory, the high-pressure calendering process in the current industrial electrode preparation process might collapse the hollow structure and weaken the structural advantages of hollow silicon anode materials. In this work, a silicon carbon composite material (Si@3DC) in which Si nanoparticles were anchored on a three-dimensional carbon framework through carbon films was prepared by a simple proton exchange method. The three-dimensional carbon framework with multiple hierarchical pores of Si@3DC was compatible with the high-pressure calendering process, but also could provide expansion space for Si nanoparticles during the lithiation process, and ensure good electronic and ionic conductivity. The carbon film on the surface of Si nanoparticles promoted the formation of stable solid electrolyte interphase (SEI) films, ensuring the good cycle stability of Si@3DC.

KEYWORDS

three-dimensional carbon framework, silicon, silicon-carbon, anode, lithium-ion battery

1 Introduction

Due to the growing consumer demand for high-energy density batteries, the current commercial graphite-based anode with a low theoretical specific capacity (372 mAh·g^{-1}) can no longer meet the requirements. Si anode with a high theoretical specific capacity (4,200 mAh·g^{-1} for Si lithiated to $Li_{4.4}Si$) has become one of the most promising candidates of the next generation anode for high energy density batteries [1–7]. However, the large volume variation of Si during discharge–charge process will lead to the pulverization of Si particles, unstable solid electrolyte interphase (SEI) film, the detachment of the active material from current collector, and eventually the loss of the interparticle electrical contact, resulting in rapid capacity decay [8–13]. In order to boost the commercialization of Si anodes, the rapid capacity decay caused by large volume variation and poor conductivity of Si must be addressed. Recently, various hollow structural designs of Si nanomaterials [14–19], such as Si@void@C [20], yolk–shell silicon carbon [21, 22], pomegranate-like Si [23], where the internal voids provided expansion space for the lithiation of Si, and the external static shell ensured the formation of stable SEI films, have successfully improved the electrochemical performance of Si anodes. However, the current industrial electrode preparation process required a high-pressure calendering process [24–29], which would collapse the hollow structure of the material and weaken the structural advantages of hollow Si anode materials. Simultaneously, the hollow structure Si-carbon materials often involved complex preparation processes, such as chemical vapor deposition and sacrificial template method [30–32], which hindered their large-scale commercial application.

Three-dimensional carbon (3DC) matrix-hosted Si nanocomposites [33–35], such as Si@3D graphene [24, 36], porous N-doped graphene@Si@hybrid silicate [37], and 3D-Si@SiO_x/C [38], could not only buffer the volume expansion of Si, but also provide good electronic and ionic conductivity, which could provide good cycling and rate performance. What is more, this kind of structure was compatible with the high-pressure calendering process in the current industrial production. In order to promote the commercialization of three-dimensional carbon matrix-hosted Si anodes, simpler and low-cost methods are still necessary to explore. In this work, the Si carbon composite material (Si@3DC) in which Si nanoparticles were anchored on a three-dimensional carbon framework through carbon films was prepared by a simple proton exchange method of deprotonating and reprotonating poly(p-phenyleneterephthalamide) (PPTA) fiber and subsequent carbonization. This method could flexibly control the distribution density of Si nanoparticles in the three-

Address correspondence to Fei Wang, wangfeihit@163.com; Mingqiang Wang, mqwang@hit.edu.cn

dimensional carbon framework. The Si nanoparticles in Si@3DC were coated and fixed in the three-dimensional carbon framework by the carbon film, instead of being only supported on the surface of the three-dimensional carbon framework. The carbon film on the surface of Si nanoparticles promoted the formation of stable SEI films and also further enhanced the electronic conductivity between the Si nanoparticles and three-dimensional carbon framework. Therefore, Si@3DC with multiple hierarchical pores and carbon film combined with Si nanoparticles could not only shorten the transport paths of ions and electrons for good electrochemical reaction kinetics, but also absorb the stress of the expansion and contraction during the (de)lithiation process of Si for a stable cycing performance. What is more, this kind of structure was compatible with the high-pressure calendering process in the current industrial production, which is conducive to the large-scale application in cylindrical and prismatic cells to achieve high energy density.

2 Experimental section

2.1 Preparation of Si@3DC

First, 1.0 wt.% PPTA solution with proton deficient state was prepared by putting PPTA fiber, KOH, and dimethyl sulfoxide (DMSO) in a sealed and dry bottle and stirring at 50 °C for 3 days (deprotonation process). Then, 70 mg Si nanoparticles and PPTA/DMSO solutions with proton deficient state were mixed uniformly by stirred and ultrasound in a sealed and dry bottle. Finally, the Si@3DC precursor was prepared by injecting the Si/PPTA/DMSO dispersion with proton deficient state into an ethanol solution containing 0.5 mol·L^{-1} HCl for a proton exchange process and followed by water washing and freeze-drying. Si@3DC precursor was carbonized at 800 °C in Ar atmosphere containing 5% H_2 to obtain Si@3DC. The preparation of 3DC was similar to that of above-mentioned Si@3DC, except that no Si nanoparticles was added. Si@C was prepared using a previously reported method [17].

2.2 Electrochemical measurement

The electrochemical performance of samples was characterized by coin-type cell with Li foil as counter electrode and Celgard 2400 separator in an electrolyte of 1 M $LiPF_6$ in a mixture of ethylene carbonate (EC) and diethyl carbonate (DEC) in a 1:1 volume ratio with 5.0 vol.% fluorinated ethylene carbonate (FEC), which was assembled in an Ar-filled glovebox. The electrode was prepared by scraping slurry of a mixing 70 wt.% active material, 15 wt.% carbon black, 7.5 wt.% carboxymethyl cellulose sodium salt, and 7.5 wt.% styrene butadiene rubber in water on thin copper foil by a scraper, followed by vacuum drying at 80 °C overnight. The Si@3DC//LFP full cells were assembled using commercialize $LiFePO_4$ (LFP) as cathode. Constant current charge and discharge test was conducted with a Neware testing system (CT-4008T-5V50mA-164, Shenzhen, China). Cyclic voltammetry (CV) and electrochemical impedance spectroscopy (EIS) tests were performed on a CHI 760E electrochemical workstation. The specific capacity of cycling and rate curves in the half cell test of Si@3DC and Si was the discharge (delithiation) specific capacity. The specific capacity of cycling and rate curves in Si@3DC//LFP full cell test was the charge (lithiation) specific capacity of LFP. The specific capacity of full cell was calculated based on the cathode active mass.

2.3 Materials characterization

The morphology of the samples was characterized by scanning electron microscopy (SEM) (Carl Zeiss Merlin Compact) and high-resolution transmission electron microscopy (HRTEM) (FEI Tecnai 30). X-ray diffraction (XRD) and X-ray photoelectron spectroscopy (XPS) were perfomed by XRD-6000 X-ray diffractometer and ESCALAB 250Xi, respectively. Thermogravimetric (TG) analysis was measured under ambient atmosphere at a heating rate of 5 °C·min^{-1} using an TA Q600 SDT Instrument. Raman spectroscopy was acquired by a confocal Raman spectroscopic system (Renishaw). The surface area and pore size distribution were obtained by the Brunauere–Emmete–Teller method (BET Quantachrome Instruments Autosorb–iQ) with the Barrett–Joyner–Halenda (BJH) method.

3 Results and discussion

Figure 1(a) presents the preparation process of Si@3DC. Firstly, a solution of deprotonated PPTA in DMSO, as shown in Fig. S1(a) in the Electronic Supplementary Material (ESM), was prepared in the KOH/DMSO system [39, 40]. Secondly, Si nanoparticles were added to this solution, and ultrasonically stirred until the dispersion was uniform (Fig. S1(b) in the ESM). Then the dispersion was squeezed into the ethanol solution by a syringe to perform the proton exchange reaction (Fig. S1(c) in the ESM) to form Si@3DC precursor. Finally, Si@3DC precursor was freeze-dried and calcined to obtain Si@3DC (Fig. 1(c) and Fig. S2 in the ESM). Analogously, a three-dimensional carbon framework in Fig. S3 in the ESM could also been prepared through the same process, except for adding Si nanoparticles (Fig. 1(b)). It was worth noting that without loaded Si nanoparticles only had a three-dimensional linear skeleton structure (Fig. S3 in the ESM). When Si nanoparticles were loaded into the three-dimensional carbon framework, the morphology of the three-dimensional carbon framework had undergone subtle changes that carbon films appeared on the surface of Si nanoparticles connecting them to the 3DC. Si nanoparticles in Si@3DC were well coated into the three-dimensional carbon framework by the carbon film (Fig. 1(c) and Fig. S2 in the ESM), instead of being only supported on the surface of three-dimensional carbon framework. The carbon film burying Si nanoparticles in the three-dimensional carbon framework had the following three functions: (1) The carbon film on the surface of Si nanoparticles could ensure the formation of stable SEI films; (2) the carbon film provided a good electronic conduction path between the Si nanoparticles and three-dimensional carbon framework; (3) the three-dimensional porous carbon framework provided expansion space for the lithiation expansion of Si nanoparticles. TEM image of Si@3DC in Fig. 1(d) shows that it was composed of amorphous carbon and crystalline Si. HRTEM image with the corresponding fast Fourier transform (FFT) of Si@3DC in Fig. 1(e) presented the high crystallinity and (111) lattice plane of Si. SEM image with corresponding energy dispersive spectroscopy (EDS) mappings of Si@3DC (Fig. S4 in the ESM) presented the uniform distribution of Si nanoparticles in the 3DC.

By adjusting the addition ratio of Si nanoparticles, the distribution density of Si nanoparticles in the three-dimensional carbon framework could be well tuned. Figures 1(f)–1(h) show SEM images of Si@3DC with different dispersion densities of Si nanoparticles prepared by dispersing 70 mg Si nanoparticles into different volumes (6, 4, and 2 mL) of deprotonated PPTA solutions. It could be seen that as the volume of the PPTA solution decreased, the Si nanoparticles in the prepared Si@3DC were more densely distributed in the 3DC. By adjusting the distribution density of Si in the three-dimensional carbon framework, it was possible to balance the electronic conductivity, the stress release during Si (de)lithiation, and the high Si content (or specific capacity), so that Si@3DC can achieve the best electrochemical

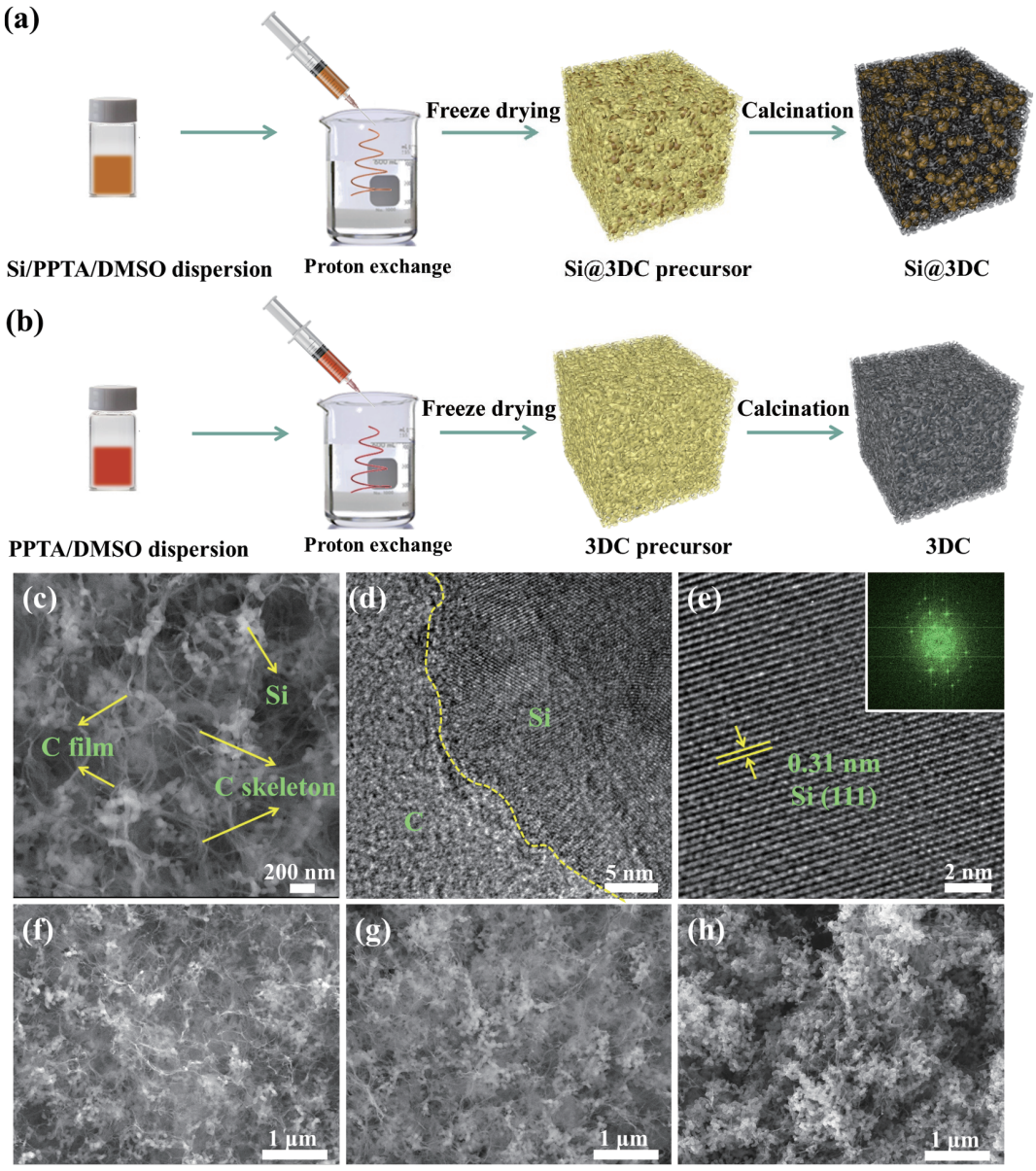

Figure 1 Preparation process and morphology characterization of the Si@3DC. Schematic illustration of the preparation process of (a) Si@3DC and (b) 3DC by the proton exchange method. (c) SEM and (d) TEM images of Si@3DC. (e) HRTEM image with the corresponding FFT of Si@3DC. SEM images of Si@3DC with different dispersion densities of Si nanoparticles prepared by dispersing 70 mg Si nanoparticles into different volumes of deprotonated PPTA solution: (f) 6 mL for Si@3DC-1, (g) 4 mL for Si@3DC-2, and (h) 2 mL for Si@3DC-3.

performance. According to the TG curves (Fig. 2(a)), it could be seen that the Si content in Si@3DC prepared with 6, 4, and 2 mL deprotonated PPTA solutions was 70.7%, 86.3%, and 95.4%, respectively.

The XRD pattern of Si@3DC (Fig. 2(b)) not only showed a good match with the XRD peak of crystalline Si, but also showed an amorphous peak at about 22° assigned to the amorphous. Raman spectra of Si@3DC (Fig. 2(c)) also presented the same conclusion as XRD pattern. XPS spectra (Fig. 2(d)) exhibited that Si@3DC had higher C signal and lower Si signal than that of Si nanoparticles, indicating that Si nanoparticles were well buried in the 3DC. Nitrogen adsorption/desorption isotherm of Si@3DC (Fig. 2(e)) exhibited a BET specific surface area of 74.5 $m^2 \cdot g^{-1}$, while the alone showed a BET surface area of 226.4 $m^2 \cdot g^{-1}$ (Fig. S5(a) in the ESM). The small specific surface area of Si@3DC could reduce the formation of SEI film to improve initial Coulombic efficiency. According to the pore size distribution of the BJH method, the average pore sizes of Si@3DC (Fig. 2(f)) and 3DC (Fig. S5(b) in the ESM) are 12.2 and 7.9 nm, respectively. The porous structure of Si@3DC could provide abundant ion transmission channels and shorten the transmission path of lithium ions, which ensured good electrochemical reaction kinetics.

The cycling performance tests of Si@3DC prepared with different dispersion densities of Si nanoparticles (Fig. S6 in the ESM) showed that Si@3DC prepared with 4 mL deprotonated PPTA solutions presented the best cycling performance, which may be due to its optimal three dimensional conductive framework structure and Si content. It should be noted that the electrochemical performance test of 3DC (Fig. S7 in the ESM) showed a reversible specific capacity of 305 $mAh \cdot g^{-1}$ at 0.5 $A \cdot g^{-1}$ after 500 cycles, which indicated that it could not only serve as a three-dimensional conductive host for Si, but also provide a part of reversible capacity. Below, Si@3DC prepared with 4 mL deprotonated PPTA solution and the control sample Si nanoparticle anodes were selected for electrochemical performance testing (Fig. 3). Si@3DC delivered a reversible specific capacity of 2,650 $mAh \cdot g^{-1}$ at 0.1 $A \cdot g^{-1}$ with an initial Coulombic efficiency of 68.8% and presented a reversible specific capacity of 1,588 $mAh \cdot g^{-1}$ with a capacity retention of 74.8% at

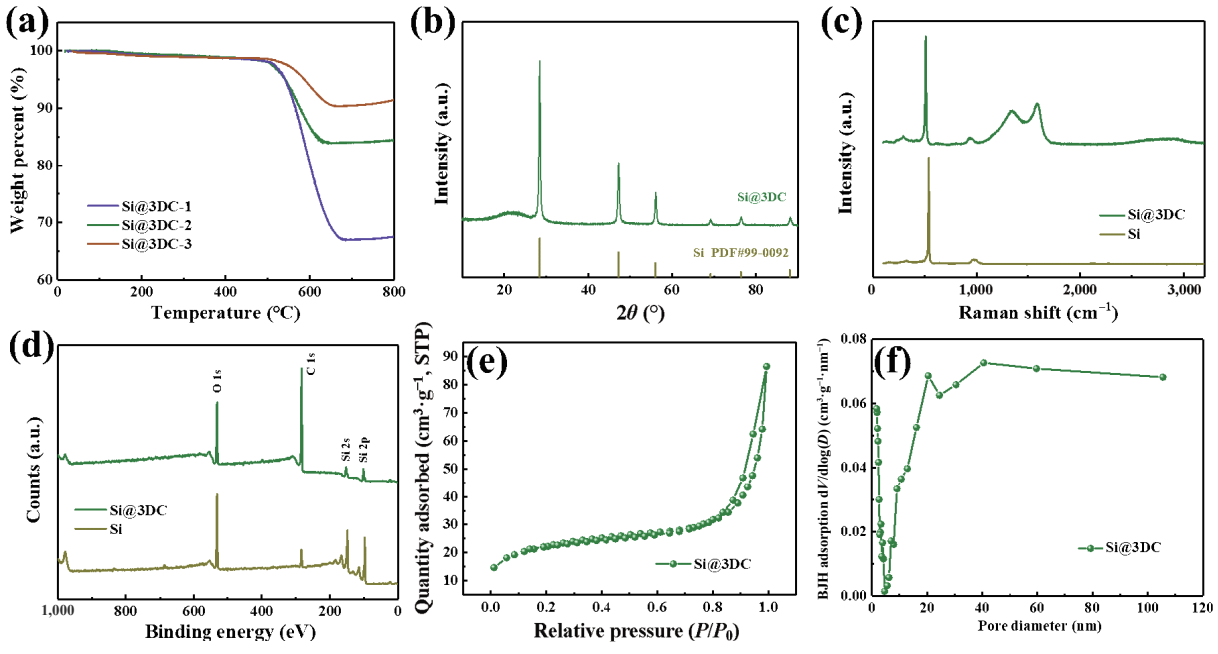

Figure 2 Characterization of the Si@3DC. (a) Thermogravimetric analyses of Si@3DC with different dispersion densities of Si nanoparticles. (b) XRD patterns, (c) Raman spectra, and (d) XPS spectra of Si@3DC and Si. (e) Adsorption/desorption isotherm and (f) BJH pore size analysis of Si@3DC.

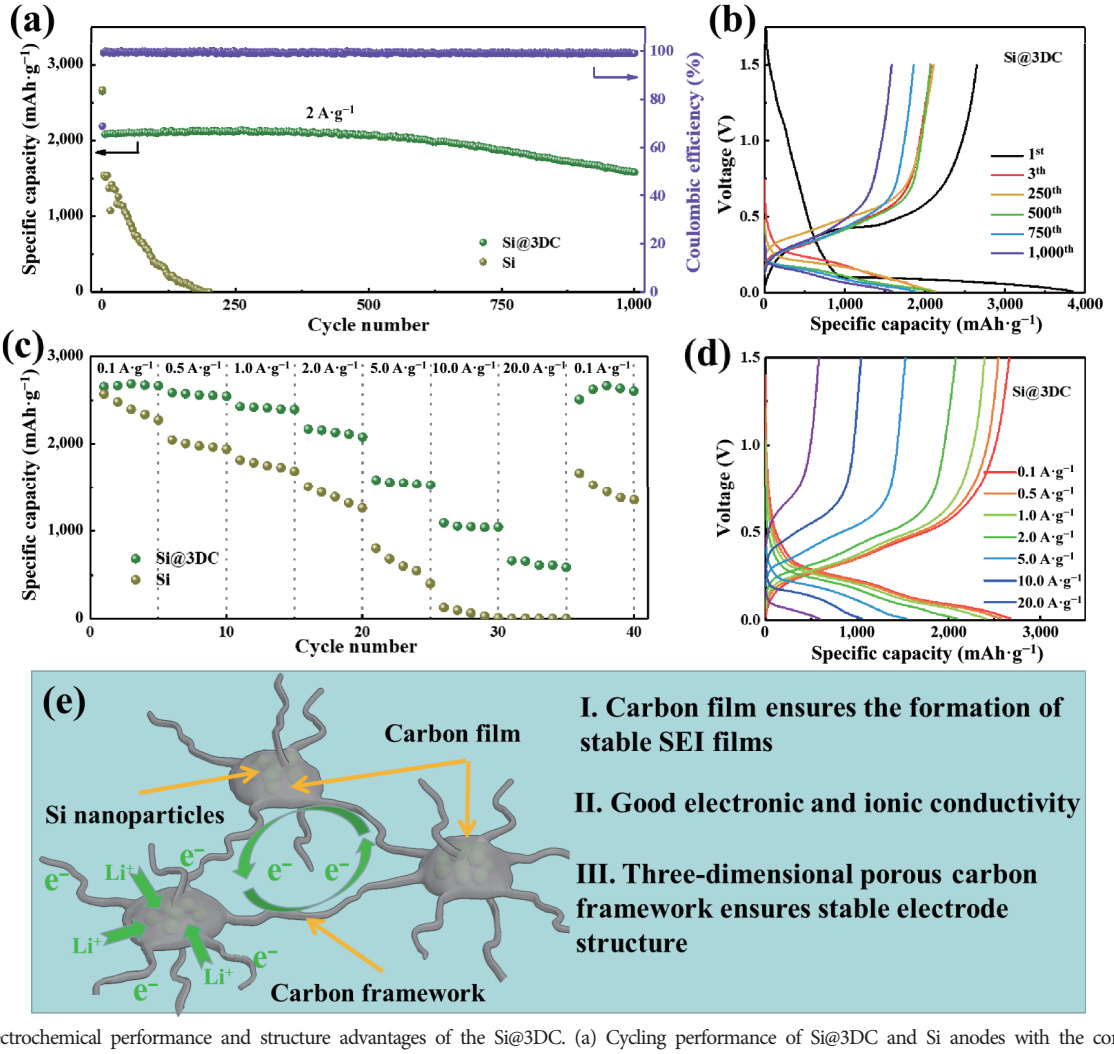

Figure 3 Electrochemical performance and structure advantages of the Si@3DC. (a) Cycling performance of Si@3DC and Si anodes with the corresponding Coulombic efficiency of the Si@3DC anode. (b) Discharge–charge curves of the Si@3DC anode at different cycles. (c) Rate performance of Si@3DC and Si anodes. (d) Discharge–charge curves of the Si@3DC anode at different rates. (e) Illustration of three functions of the Si@3DC structure: I. The carbon film on the surface of Si nanoparticles could ensure the formation of stable SEI films; II. the carbon films bound Si nanoparticles to the porous three-dimensional carbon framework, providing good electronic and ionic conduction pathways; III. the three-dimensional porous carbon framework provided expansion space for the lithiation expansion of Si nanoparticles, avoiding the collapse of the electrode structure.

2 A·g^{-1} after 1,000 cycles (Fig. 3(a)). As a control, Si nanoparticle anodes exhibited a rapid decay capacity and the capacity decayed to almost zero at 2 A·g^{-1} after 200 cycles. As the number of cycles increased, the charge–discharge curves of Si@3DC anode presented smaller polarization than that of Si nanoparticle anodes (Fig. 3(b) and Fig. S8 in the ESM), which indicated that the Si@3DC anode had good electrochemical reaction kinetics. To further illustrate the good cycling stability of Si@3DC, the cycling performance of Si@C (Fig. S9 in the ESM) as a control was also tested. Si@C with a carbon-coated structure exhibited poorer cycling stability than that of Si@3DC, indicating that the structure of Si nanoparticles fixed on the three-dimensional carbon frame by carbon film was beneficial to the improvement of electrochemical performance compared with carbon coating alone. As shown in the Fig. 3(c), the Si@3DC anode exhibited excellent rate capacity of 1,554, 1,056, and 658 mAh·g^{-1} at rates of 5.0, 10.0, and 20.0 A·g^{-1}, respectively, which could be attributed to the porous three-dimensional carbon conductive framework that provided fast ionic and electronic conduction paths. However, Si nanoparticle anode exhibited poor rate capacities of 602, 101, and 8 mAh·g^{-1} at rates of 5.0, 10.0, and 20.0 A·g^{-1}, respectively. Figure 3(d) presented the representative rate charge–discharge curves of Si@3DC anode. The good electrochemical performance of Si@3DC anode was attributed to the following three functions of the Si@3DC structure, as shown in Fig. 3(e): (1) The carbon film on the surface of Si nanoparticles could ensure the formation of stable SEI films; (2) the carbon films bound Si nanoparticles to the porous three-dimensional carbon framework, providing good electronic and ionic conduction pathways; (3) the three-dimensional porous carbon framework provided expansion space for the lithiation expansion of Si nanoparticles, avoiding the collapse of the electrode structure.

The morphology of Si@3DC and Si nanoparticle anodes after 200 cycles at 2 A·g^{-1} was characterized, as shown in Fig. S10 in the ESM. It could be observed that Si@3DC active materials were still well combined with the current collector after cycling (Fig. S10(a) in the ESM), and there were no microcracks on the surface of Si@3DC anode (Fig. S10(b) in the ESM). However, the surface of Si nanoparticle anode cracked after cycling, and the active materials fell off from the current collector (Figs. S10(d) and S10(e) in the ESM). The excellent mechanical performance of Si@3DC anode was attributed to the porous three-dimensional carbon framework which can provide a buffer space for the volume change of Si during (de)lithiation. The high magnification SEM image showed that the surface of Si@3DC anode presented thinner SEI films after cycling (Fig. S10(c) in the ESM), while Si nanoparticle anode exhibited thicker SEI films (Fig. S10(f) in the ESM). This indicated that the carbon films on the surface of Si nanoparticles in the Si@3DC anode promoted the formation of stable SEI films.

In order to better understand the good electrochemical performance of Si@3DC, the *in-situ* electrochemical behavior of Si@3DC and blank control Si nanoparticle anodes were investigated, as shown in Fig. 4. The differential capacitance (dQ_m/dV) curves of Si@3DC (Fig. 4(a)) and Si nanoparticle (Fig. 4(b)) anodes demonstrated two lithiation processes of Si at potentials of 0.17 and 0.05 V, and two delithiation processes of Si at potentials of 0.32 and 0.51 V [41–44]. As the number of cycles increases, the peak of dQ_m/dV curves of Si@3DC anode decayed much slower than that of Si anode, indicating good cycling stability of Si@3DC. The CV curves of Si@3DC anode at different scanning speeds (Fig. 4(c)) presented more regular increasing peaks than those of Si anode at different scanning speeds (Fig. 4(d)), indicating good rate performance of Si@3DC. According to Eq. (S2) in the ESM and the relationship between the peak current (I_p) and the square root of scanning speeds ($v^{1/2}$) (Fig. 4(e)), the lithium ion transfer coefficient (D_{Li^+}) of Si@3DC anode was calculated to be 1.95 times of that value of Si nanoparticle anode [45–47]. Galvanostatic intermittent titration technique (GITT) was also used to further investigate D_{Li^+} of Si@3DC and Si nanoparticle anodes during different states of charge [48–51]. The D_{Li^+} of Si@3DC and Si nanoparticle anodes during different states

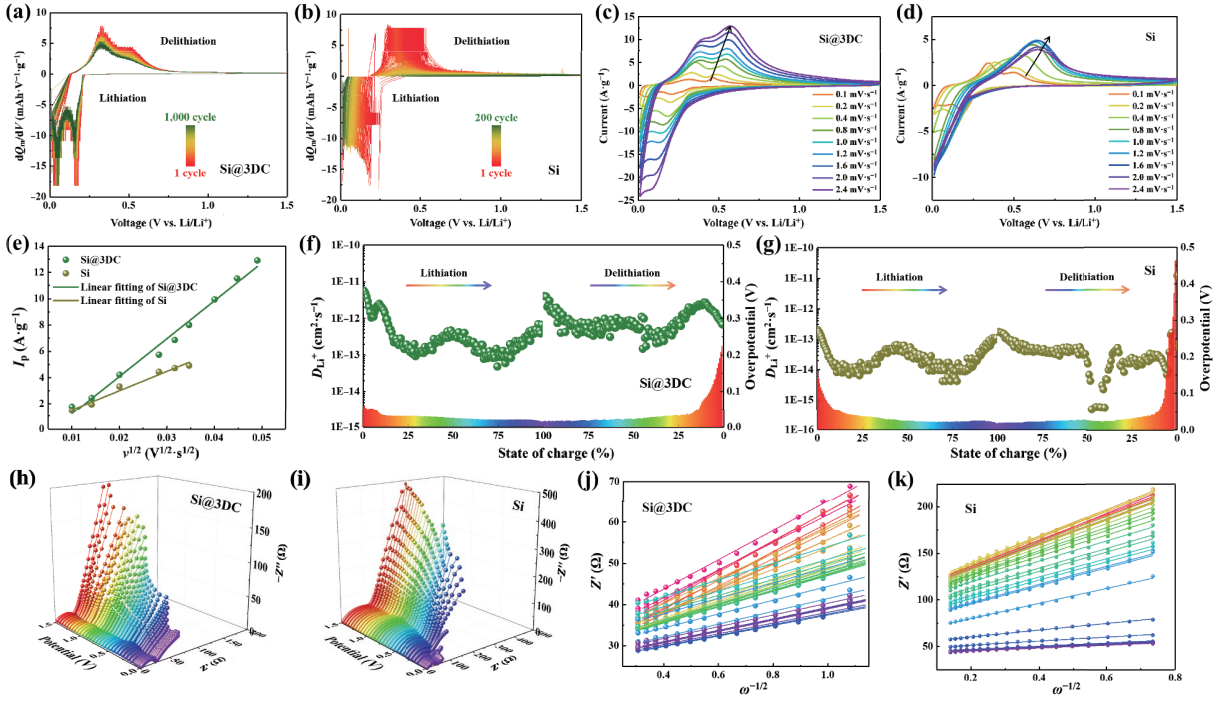

Figure 4 Electrochemical behavior of the Si@3DC. The dQ_m/dV curves of (a) Si@3DC and (b) Si anodes at 2.0 A·g^{-1} for different cycles. CV profiles of (c) Si@3DC and (d) Si anodes at different scanning speeds. (e) Relationship between the CV I_p and $v^{1/2}$ for Si@3DC and Si anodes. The D_{Li^+} and overpotential of (f) Si@3DC and (g) Si anodes during the (de)lithiation process. EIS curves of (h) Si@3DC and (i) Si anodes at different potentials. Relationship between Z' and $\omega^{-1/2}$ of (j) Si@3DC and (k) Si anodes in low frequency section.

of charge calculated by the GITT curves (Fig. S11 in the ESM) were presented in Figs. 4(f) and 4(g). It could be seen that Si@3DC anode had higher D_{Li^+} value than that of Si nanoparticle anode in different charged states. In detail, the average D_{Li^+} of Si@3DC anode in lithiation and delithiation process were 9.4×10^{-13} and 1.1×10^{-12} $cm^2 \cdot s^{-1}$, while the average D_{Li^+} of Si anode in lithiation and delithiation process were 3.1×10^{-14} and 1.3×10^{-13} $cm^2 \cdot s^{-1}$, respectively. EIS tests at different potentials (Figs. 4(h) and 4(i)) demonstrated that Si@3DC anode had a smaller electrochemical reaction impedance (R_{ct}) than Si nanoparticle anode, indicating good electrochemical reaction kinetics of Si@3DC anode. According to the relationship between the real part of impedance (Z') and angular frequency ($\omega^{-1/2}$) (Figs. 4(j) and 4(k)) in the EIS low frequency region [52, 53], the D_{Li^+} ratios of Si@3DC and Si nanoparticle anodes were calculated to be about 1.5–6 (Fig. S12 in the ESM) at different potentials, indicating that Si@3DC anode had fast lithium ion transport channels.

The electrochemical performance of full cell (Fig. S13 in the ESM) composed of the activated Si@3DC anode and the commercial LFP cathode had also been investigated. The Si@3DC//LFP full cell exhibited a reversible specific capacity of 129 $mAh \cdot g^{-1}$ with a capacity retention of 95.9% at a current density of 1 C (170 $mA \cdot g^{-1}$) after 200 cycles (Fig. 5(a)). It could be seen from the charge and discharge curves of the full cell at different cycles (Fig. 5(b)) that as the number of cycles increased, the full cell exhibited a small polarization. The full cell exhibited a high rate capacity of 119 $mAh \cdot g^{-1}$ at 2 C (Fig. 5(c)). The representative charge and discharge curves of the full cell at different rates were shown in Fig. 5(d). The excellent performance of Si@3DC//LFP full cell indicated the good application potential of Si@3DC anode.

4 Conclusions

In conclusion, Si@3DC was prepared by a simple proton exchange method. This method could flexibly control the distribution density of Si nanoparticles in the three-dimensional carbon framework. The Si nanoparticles in Si@3DC were anchored to the three-dimensional carbon framework by the carbon film, providing good electronic and ionic conductivity and promoting the formation of stable SEI film. Simultaneously, the three-dimensional carbon network with multiple hierarchical pores could provide expansion space for Si nanoparticles during the lithiation process, ensuring the stable electrode structure. What's more, this kind of structure was compatible with the high-pressure calendering process in the current industrial production, which was conducive to the large-scale application in cylindrical and prismatic cells to achieve high energy density. Si@3DC presented an excellent cycling performance of 1,588 $mAh \cdot g^{-1}$ with a capacity retention of 74.8% at 2 $A \cdot g^{-1}$ after 1,000 cycles, and a splendid rate performance of 1,554, 1,056, and 658 $mAh \cdot g^{-1}$ at rates of 5.0, 10.0, and 20.0 $A \cdot g^{-1}$, respectively. In addition, this construction method of three-dimensional carbon framework loaded nanoparticles anchored by carbon film was scalable for many other energy storage materials, because this method was decoupled from properties of active materials.

Acknowledgements

This work was supported financially by the National Key Research and Development Program of China (No. 2017YFB0307701).

Electronic Supplementary Material: Supplementary material (digital photographs of PPTA/DMSO solutions, Si/PPTA/DMSO solutions, and proton exchange process (Fig. S1); TEM, SEM, and EDS of Si@3DC and 3DC (Figs. S2–S4); N_2 sorption isotherm and BJH analysis of 3DC (Fig. S5); cycling performance of Si@3DC and 3DC (Figs. S6 and S7); charge–discharge curves of Si anode at different cycling (Fig. S8); TEM image and cycling performance of Si@C (Fig. S9); morphology of Si@3DC and Si nanoparticle anodes (Fig. S10); GITT plots D_{Li^+} ratio of Si@3DC and Si nanoparticle anodes (Figs. S11 and S12); schematic diagram (Fig. S13) of the Si@3DC//LFP full cell) is available in the online version of this article at https://doi.org/10.1007/s12274-022-4264-z.

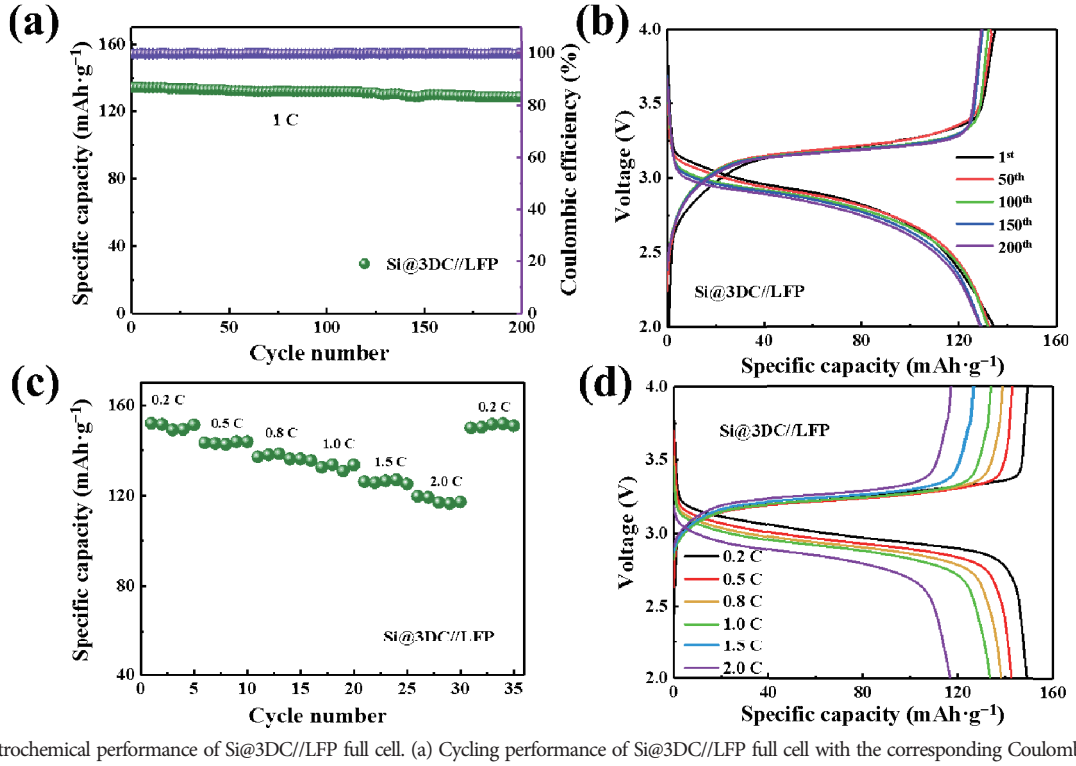

Figure 5 Electrochemical performance of Si@3DC//LFP full cell. (a) Cycling performance of Si@3DC//LFP full cell with the corresponding Coulombic efficiency at 1 C. (b) Discharge–charge profiles of Si@3DC//LFP full cell at different cycles. (c) Rate performance of Si@3DC//LFP full cell. (d) Discharge–charge curves of Si@3DC//LFP full cell at different rates.

References

[1] Jia, H. P.; Li, X. L.; Song, J. H.; Zhang, X.; Luo, L. L.; He, Y.; Li, B. S.; Cai, Y.; Hu, S. Y.; Xiao, X. C. et al. Hierarchical porous silicon structures with extraordinary mechanical strength as high-performance lithium-ion battery anodes. *Nat. Commun.* **2020**, *11*, 1474.

[2] Sung, J.; Kim, N.; Ma, J.; Lee, J. H.; Joo, S. H.; Lee, T.; Chae, S.; Yoon, M.; Lee, Y.; Hwang, J. et al. Subnano-sized silicon anode via crystal growth inhibition mechanism and its application in a prototype battery pack. *Nat. Energy* **2021**, *6*, 1164–1175.

[3] Jeong, Y. K.; Huang, W.; Vilá, R. A.; Huang, W. X.; Wang, J. Y.; Kim, S. C.; Kim, Y. S.; Zhao, J.; Cui, Y. Microclusters of kinked silicon nanowires synthesized by a recyclable iodide process for high-performance lithium-ion battery anodes. *Adv. Energy Mater.* **2020**, *10*, 2002108.

[4] Wang, F.; Wang, B.; Li, J. X.; Wang, B.; Zhou, Y.; Wang, D. L.; Liu, H. K.; Dou, S. X. Prelithiation: A crucial strategy for boosting the practical application of next-generation lithium ion battery. *ACS Nano.* **2021**, *15*, 2197–2218.

[5] Xiang, B.; An, W. L.; Fu, J. J.; Mei, S. X.; Guo, S. G.; Zhang, X. M.; Gao, B.; Chu, P. K. Graphene-encapsulated blackberry-like porous silicon nanospheres prepared by modest magnesiothermic reduction for high-performance lithium-ion battery anode. *Rare Metals* **2021**, *40*, 383–392.

[6] Zhang, F. Z.; Ma, Y. Y.; Jiang, M. M.; Luo, W.; Yang, J. P. Boron heteroatom-doped silicon-carbon peanut-like composites enables long life lithium-ion batteries. *Rare Metals* **2022**, *41*, 1276–1283.

[7] Xu, Q.; Li, J. Y.; Sun, J. K.; Yin, Y. X.; Wan, L. J.; Guo, Y. G. Watermelon-inspired Si/C microspheres with hierarchical buffer structures for densely compacted lithium-ion battery anodes. *Adv. Energy Mater.* **2017**, *7*, 1601481.

[8] Zhang, X. H.; Wang, D. H.; Qiu, X. Y.; Ma, Y. J.; Kong, D. B.; Müllen, K.; Li, X. L.; Zhi, L. J. Stable high-capacity and high-rate silicon-based lithium battery anodes upon two-dimensional covalent encapsulation. *Nat. Commun.* **2020**, *11*, 3826.

[9] Wang, J. Y.; Cui, Y. Electrolytes for microsized silicon. *Nat. Energy* **2020**, *5*, 361–362.

[10] Mu, T. S.; Shen, B. C.; Lou, S. F.; Zhang, Z. G.; Ren, Y.; Zhou, X. M.; Zuo, P. J.; Du, C. Y.; Ma, Y. L.; Huo, H. et al. Scalable mesoporous silicon microparticles composed of interconnected nanoplates for superior lithium storage. *Chem.—Eng. J.* **2019**, *375*, 121923.

[11] Zeng, K.; Li, T.; Qin, X. Y.; Liang, G. M.; Zhang, L. H.; Liu, Q.; Li, B. H.; Kang, F. Y. A combination of hierarchical pore and buffering layer construction for ultrastable nanocluster Si/SiO_x anode. *Nano Res.* **2020**, *13*, 2987–2993.

[12] Liu, N. T.; Liu, J.; Jia, D. Z.; Huang, Y. D.; Luo, J.; Mamat, X.; Yu, Y.; Dong, Y. M.; Hu, G. Z. Multi-core yolk–shell like mesoporous double carbon-coated silicon nanoparticles as anode materials for lithium-ion batteries. *Energy Storage Mater.* **2019**, *18*, 165–173.

[13] Mu, T. S.; Zhao, Y.; Zhao, C. T.; Holmes, N. G.; Lou, S. F.; Li, J. J.; Li, W. H.; He, M. X.; Sun, Y. P.; Du, C. Y. et al. Stable silicon anodes by molecular layer deposited artificial zincone coatings. *Adv. Funct. Mater.* **2021**, *31*, 2010526.

[14] Liu, H. B.; Chen, Y.; Jiang, B.; Zhao, Y.; Guo, X. L.; Ma, T. L. Hollow-structure engineering of a silicon-carbon anode for ultra-stable lithium-ion batteries. *Dalton Trans.* **2020**, *49*, 5669–5676.

[15] Xue, H. J.; Wu, Y. Q.; Wang, Z. M.; Shen, Y. B.; Sun, Q. J.; Liu, G.; Yin, D. M.; Wang, L. M.; Li, Q.; Ming, J. Unraveling the new role of metal-organic frameworks in designing silicon hollow nanocages for high-energy lithium-ion batteries. *ACS Appl. Mater. Interfaces* **2021**, *13*, 40471–40480.

[16] Yi, Y.; Lee, G. H.; Kim, J. C.; Shim, H. W.; Kim, D. W. Tailored silicon hollow spheres with *Micrococcus* for Li-ion battery electrodes. *Chem.—Eng. J.* **2017**, *327*, 297–306.

[17] Wan, X. H.; Tang, Z. H.; Chen, J. L.; Xue, Y. C.; Zhang, J. H.; Guo, X. M.; Liu, Y. J.; Kong, Q. H.; Yuan, A. H.; Fan, H. Molten salt-assisted magnesiothermic reduction synthesis of spherical Si hollow structure as promising anode materials of lithium ion batteries. *Chem. Lett.* **2019**, *48*, 1547–1550.

[18] Ma, T. Y.; Yu, X. N.; Li, H. Y.; Zhang, W. G.; Cheng, X. L.; Zhu, W. T.; Qiu, X. P. High volumetric capacity of hollow structured SnO_2@Si nanospheres for lithium-ion batteries. *Nano Lett.* **2017**, *17*, 3959–3964.

[19] Wang, J. Y.; Cui, Y.; Wang, D. Design of hollow nanostructures for energy storage, conversion and production. *Adv. Mater.* **2019**, *31*, 1801993.

[20] Wang, F.; Wang, B.; Ruan, T. T.; Gao, T. T.; Song, R. S.; Jin, F.; Zhou, Y.; Wang, D. L.; Liu, H. K.; Dou, S. X. Construction of structure-tunable Si@void@C anode materials for lithium-ion batteries through controlling the growth kinetics of resin. *ACS Nano.* **2019**, *13*, 12219–12229.

[21] Liu, N.; Wu, H.; McDowell, M. T.; Yao, Y.; Wang, C. M.; Cui, Y. A yolk–shell design for stabilized and scalable Li-ion battery alloy anodes. *Nano Lett.* **2012**, *12*, 3315–3321.

[22] Chen, S. R.; Gordin, M. L.; Yi, R.; Howlett, G.; Sohn, H.; Wang, D. H. Silicon core–hollow carbon shell nanocomposites with tunable buffer voids for high capacity anodes of lithium-ion batteries. *Phys. Chem. Chem. Phys.* **2012**, *14*, 12741–12745.

[23] Liu, N.; Lu, Z. D.; Zhao, J.; McDowell, M. T.; Lee, H. W.; Zhao, W. T.; Cui, Y. A pomegranate-inspired nanoscale design for large-volume-change lithium battery anodes. *Nat. Nanotechnol.* **2014**, *9*, 187–192.

[24] Son, Y.; Kim, N.; Lee, T.; Lee, Y.; Ma, J.; Chae, S.; Sung, J.; Cha, H.; Yoo, Y.; Cho, J. Calendering-compatible macroporous architecture for silicon-graphite composite toward high-energy lithium-ion batteries. *Adv. Mater.* **2020**, *32*, 2003286.

[25] Zhu, G. J.; Chao, D. L.; Xu, W. L.; Wu, M. H.; Zhang, H. J. Microscale silicon-based anodes: Fundamental understanding and industrial prospects for practical high-energy lithium-ion batteries. *ACS Nano* **2021**, *15*, 15567–15593.

[26] Feng, L. X.; Ji, Y.; Zhu, Z. W.; Yu, P.; Fu, X. W.; Yang, M.; Wang, Y.; Yang, W. Rational design and superfast production of biomimetic, calendering-compatible, catalytic, sulfur-rich secondary particles for advanced lithium-sulfur batteries. *Energy Storage Mater.* **2021**, *40*, 415–425.

[27] Ge, M. Z.; Cao, C. Y.; Biesold, G. M.; Sewell, C. D.; Hao, S. M.; Huang, J.; Zhang, W.; Lai, Y. K.; Lin, Z. Q. Recent advances in silicon-based electrodes: From fundamental research toward practical applications. *Adv. Mater.* **2021**, *33*, 2004577.

[28] Smekens, J.; Gopalakrishnan, R.; Steen, N. V. D.; Omar, N.; Hegazy, O.; Hubin, A.; Van Mierlo, J. Influence of electrode density on the performance of Li-ion batteries: Experimental and simulation results. *Energies* **2016**, *9*, 104.

[29] Meyer, C.; Bockholt, H.; Haselrieder, W.; Kwade, A. Characterization of the calendering process for compaction of electrodes for lithium-ion batteries. *J. Mater. Process. Technol.* **2017**, *249*, 172–178.

[30] Zhu, R. Y.; Hu, X. J.; Chen, K.; Dang, J.; Wang, X. J.; Liu, X. J.; Wang, H. Double-shelled hollow carbon nanospheres as enclosed electrochemical reactors to enhance the lithium storage performance of silicon nanodots. *J. Mater. Chem. A* **2020**, *8*, 12502–12517.

[31] Tian, H.; Tian, H. J.; Yang, W.; Zhang, F.; Yang, W.; Zhang, Q. B.; Wang, Y.; Liu, J.; Silva, S. R. P.; Liu, H. et al. Stable hollow-structured silicon suboxide-based anodes toward high-performance lithium-ion batteries. *Adv. Funct. Mater.* **2021**, *31*, 2101796.

[32] Xie, J.; Tong, L.; Su, L. W.; Xu, Y. W.; Wang, L. B.; Wang, Y. H. Core–shell yolk–shell Si@C@void@C nanohybrids as advanced lithium ion battery anodes with good electronic conductivity and corrosion resistance. *J. Power Sources* **2017**, *342*, 529–536.

[33] Wang, H. W.; Fu, J. Z.; Wang, C.; Wang, J. W.; Yang, A. K.; Li, C. C.; Sun, Q. F.; Cui, Y.; Li, H. Q. A binder-free high silicon content flexible anode for Li-ion batteries. *Energy Environ. Sci.* **2020**, *13*, 848–858.

[34] Ren, W. F.; Li, J. T.; Huang, Z. G.; Deng, L.; Zhou, Y.; Huang, L.; Sun, S. G. Fabrication of Si nanoparticles@conductive carbon framework@polymer composite as high-areal-capacity anode of lithium-ion batteries. *ChemElectroChem* **2018**, *5*, 3258–3265.

[35] Harpak, N.; Davidi, G.; Schneier, D.; Menkin, S.; Mados, E.; Golodnitsky, D.; Peled, E.; Patolsky, F. Large-scale self-catalyzed spongelike silicon nano-network-based 3D anodes for high-capacity lithium-ion batteries. *Nano Lett.* **2019**, *19*, 1944–1954.

[36] Chang, P.; Liu, X. X.; Zhao, Q. J.; Huang, Y. Q.; Huang, Y. H.; Hu, X. L. Constructing three-dimensional honeycombed graphene/silicon skeletons for high-performance Li-ion batteries. *ACS Appl. Mater. Interfaces* **2017**, *9*, 31879–31886.

[37] Huang, G.; Han, J. H.; Lu, Z.; Wei, D. X.; Kashani, H.; Watanabe, K.; Chen, M. W. Ultrastable silicon anode by three-dimensional nanoarchitecture design. *ACS Nano* **2020**, *14*, 4374–4382.

[38] Lee, J.; Moon, J.; Han, S. A.; Kim, J.; Malgras, V.; Heo, Y. U.; Kim, H.; Lee, S. M.; Liu, H. K.; Dou, S. X. et al. Everlasting living and breathing gyroid 3D network in Si@SiO_x/C nanoarchitecture for lithium ion battery. *ACS Nano* **2019**, *13*, 9607–9619.

[39] He, Z. C.; Wu, F.; Guan, S. J.; Liu, L.; Li, J.; Huang, Y. D. Polyamide amine/aramid nanofiber composite aerogels as an ultra-high capacity adsorbent for Congo red removal. *J. Mater. Chem. A* **2021**, *9*, 13320–13331.

[40] Yang, B.; Wang, L.; Zhang, M. Y.; Li, W. W.; Zhou, Q. K.; Zhong, L. X. Advanced separators based on aramid nanofiber (ANF) membranes for lithium-ion batteries: A review of recent progress. *J. Mater. Chem. A* **2021**, *9*, 12923–12946.

[41] Mu, T. S.; Lou, S. F.; Holmes, N. G.; Wang, C. H.; He, M. X.; Shen, B. C.; Lin, X. T.; Zuo, P. J.; Ma, Y. L.; Li, R. Y. et al. Reversible silicon anodes with long cycles by multifunctional volumetric buffer layers. *ACS Appl. Mater. Interfaces* **2021**, *13*, 4093–4101.

[42] Salah, M.; Hall, C.; De Eulate, E. A.; Murphy, P.; Francis, C.; Kerr, R.; Pathirana, T. Fabretto, M. Compressively stressed silicon nanoclusters as an antifracture mechanism for high-performance lithium-ion battery anodes. *ACS Appl. Mater. Interfaces* **2020**, *12*, 39195–39204.

[43] Liang, G. M.; Qin, X. Y.; Zou, J. S.; Luo, L. Y.; Wang, Y. Z.; Wu, M. Y.; Zhu, H.; Chen, G. H.; Kang, F. Y.; Li, B. H. Electrosprayed silicon-embedded porous carbon microspheres as lithium-ion battery anodes with exceptional rate capacities. *Carbon* **2018**, *127*, 424–431.

[44] Yang, Z. W.; Wu, C.; Li, S.; Qiu, L.; Yang, Z. G.; Zhong, Y. J.; Zhong, B. H.; Song, Y.; Wang, G. K.; Liu, Y. X. et al. A unique structure of highly stable interphase and self-consistent stress distribution radial-gradient porous for silicon anode. *Adv. Funct. Mater.* **2021**, 2107897.

[45] Chen, X. X.; Ge, G. F.; Wang, W. Y.; Zhang, B.; Jiang, J. J.; Yang, X. L.; Li, Y. Z.; Wang, L.; He, X. M.; Sun, Y. M. *In situ* formation of ionically conductive nanointerphase on Si particles for stable battery anode. *Sci. China Chem.* **2021**, *64*, 1417–1425.

[46] Li, W. L.; Chen, K.; Xu, Q. C.; Li, X. Y.; Zhang, Q.; Weng, J.; Xu, J. Mo_2C/C hierarchical double-shelled hollow spheres as sulfur host for advanced Li-S batteries. *Angew. Chem., Int. Ed.* **2021**, *60*, 21512–21520.

[47] Wang, W. C.; Liang, H. C.; Zhang, L.; Savilov, S. V.; Ni, J. F.; Li, L. Carbon nanotube directed three-dimensional porous Li_2FeSiO_4 composite for lithium batteries. *Nano Res.* **2017**, *10*, 229–237.

[48] Han, M.; Lin, Z.; Ji, X.; Mu, Y.; Li, J.; Yu, J. Growth of flexible and porous surface layers of vertical graphene sheets for accommodating huge volume change of silicon in lithium-ion battery anodes. *Mater. Today Energy* **2020**, *17*, 100445.

[49] Zeng, W. W.; Wang, L.; Peng, X.; Liu, T. F.; Jiang, Y. Y.; Qin, F.; Hu, L.; Chu, P. K.; Huo, K. F.; Zhou, Y. H. Enhanced ion conductivity in conducting polymer binder for high-performance silicon anodes in advanced lithium-ion batteries. *Adv. Energy Mater.* **2018**, *8*, 1702314.

[50] Meng, T.; Li, B.; Wang, Q. S.; Hao, J. N.; Huang, B. B.; Gu, F. L.; Xu, H. M.; Liu, P.; Tong, Y. X. Large-scale electric-field confined silicon with optimized charge-transfer kinetics and structural stability for high-rate lithium-ion batteries. *ACS Nano* **2020**, *14*, 7066–7076.

[51] Li, P. C.; Chen, G.; Zhang, N.; Ma, R. Z.; Liu, X. H. β-cyclodextrin as lithium-ion diffusion channel with enhanced kinetics for stable silicon anode. *Energy Environ. Mater.* **2021**, *4*, 72–80.

[52] Chen, M.; Zhou, Q. N.; Zai, J. T.; Iqbal, A.; Tsega, T.; Dong, B. X.; Liu, X. J.; Zhang, Y. C.; Yan, C. Y.; Zhao, L. et al. High power and stable P-doped yolk–shell structured Si@C anode simultaneously enhancing conductivity and Li^+ diffusion kinetics. *Nano Res.* **2021**, *14*, 1004–1011.

[53] Ge, M. Y.; Wi, S.; Liu, X.; Bai, J. M.; Ehrlich, S.; Lu, D. Y.; Lee, W. K.; Chen, Z. H.; Wang, F. Kinetic limitations in single-crystal high-nickel cathodes. *Angew. Chem., Int. Ed.* **2021**, *60*, 17350–17355.